RECENT RESULTS FROM THE SPITZER SPACE TELESCOPE: A NEW VIEW OF THE INFRARED UNIVERSE

Giovanni G. Fazio
Harvard-Smithsonian Center for Astrophysics, 60 Garden Street, Cambridge, MA 02138, USA

Abstract The *Spitzer Space Telescope*, NASA's Great Observatory for infrared exploration, was launched on August 25, 2003, and is returning excellent scientific data. Combining the intrinsic sensitivity obtained with a cooled telescope in space and the imaging and spectroscopic power of modern array detectors, huge gains have been achieved in exploring the infrared universe. This paper describes the *Spitzer Space Telescope* and its focal-plane instruments and summarizes some of the spectacular images and new scientific results that have been obtained.

Keywords: infrared – galaxy classification – interstellar dust – star formation – interacting galaxies – active galactic nuclei – planetary nebula

1. Introduction

Infrared astronomy, which covers the wavelength region from 1 to 1000 μm, is concerned primarily with the study of relatively cold objects in the universe with temperatures ranging from a few degrees Kelvin to about 2000 K. One principal source of infrared radiation in the interstellar medium is dust, which absorbs optical and ultraviolet radiation and reradiates at infrared wavelengths. Infrared observations can also penetrate dust-enshrouded sources, which are invisible to optical and ultraviolet radiation. Observations of the early universe at infrared wavelengths have the advantage of seeing galaxies whose optical light has been redshifted into the infrared.

However, when using ground-based telescopes, most of the infrared spectrum in invisible because of atmospheric absorption (Figure 1). Only a few windows from 1 to 30 μm wavelength are available. Also because of thermal emission from the atmosphere and from the telescope, the background infrared radiation is relatively high, making ground-based observations very difficult.

By placing an infrared telescope in space, atmospheric emission and absorption can be eliminated and, in addition, the telescope can be cooled to eliminate

the thermal background radiation. With a cooled telescope in space the infrared background radiation is due only to the scattered and thermal emission from the zodiacal dust in our solar system. The reduction in background radiation that can be achieved is rather dramatic, a factor of 1 million (Figure 1).

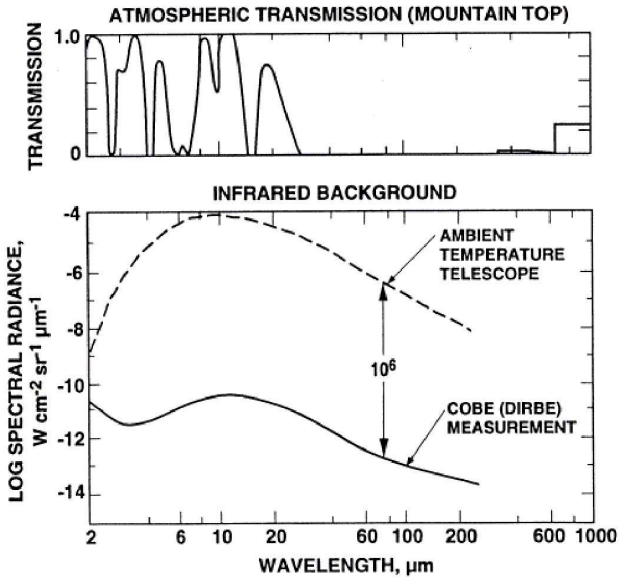

Figure 1. The top figure is a plot of the earth's atmospheric transmission versus infrared wavelength, and the lower figure is a plot the infrared background radiation versus infrared wavelength for a ground-based telescope and helium-cooled space telescope.

The following sections will describe the *Spitzer Space Telescope* and its three focal plane instruments and present a sample of the spectacular images and scientific results that have been produced.

2. Spitzer Space Telescope

NASA's *Infrared Astronomy Satellite (IRAS),* which was launched in 1985, consisted of a liquid-helium cooled telescope (60-cm mirror) and produced the first all-sky maps of the infrared universe at 25, 60, and 100 μm wavelength. *IRAS* was followed in 1996 with another cooled telescope in space, the *Infrared Satellite Observatory (ISO),* an ESA mission, which was a true observatory that could carry out follow-up observations of the *IRAS* sources. In 2003, NASA's *Spitzer Space Telescope*, with an 85-cm mirror, achieved major advances in sensitivity, image quality and field-of-view over *ISO*. Although its mirror was only slightly larger than *ISO's* 60-cm mirror, the use of new, sensitive, and large-area infrared array detectors has permitted this new view of the infrared universe.

The *Spitzer Space Telescope*, NASA's Great Observatory for infrared exploration, was launched on 2003 August 25, into a heliocentric orbit, trailing the Earth (Figure 2). The telescope consists of an 85-cm cryogenically-cooled mirror and three focal-plane instruments, which provide background-limited imaging and spectroscopy covering the spectral region from 3 to 180μm wavelength. Incorporating large-format infrared detector arrays, with the intrinsic sensitivity of a cryogenic telescope, and the high observing efficiency of a solar orbit, Spitzer has already demonstrated dramatic improvements in capability over previous infrared space missions. Following 60 days of In-Orbit-Checkout and 30 days of Science Verification, normal operations began on 2003 December 1. To date, all spacecraft systems continue to operate extremely well (Werner et al. 2004). The Telescope has an expected lifetime of 5 to 6 years. More than 75% of the observing time will be available for General Observers.

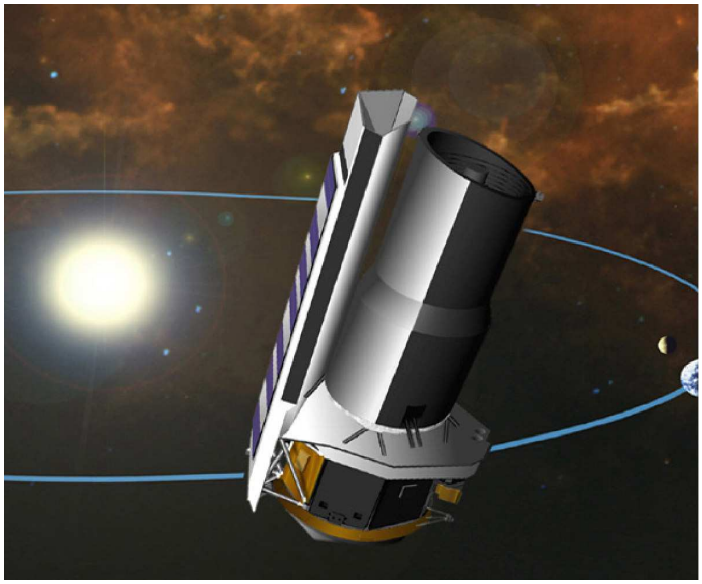

Figure 2. Artist's conception of the Spitzer Space Telescope in earth-trailing solar orbit.

Two of the *Spitzer Space Telescope* instruments, the Infrared Array Camera (IRAC; Fazio et al. 2004), and the Multiband Infrared Photometer for Spitzer (MIPS; Rieke et al. 2004) are designed as imaging instruments, although the MIPS also has a spectral energy distribution (SED) channel for very low-resolution spectroscopy. IRAC covers the wavelength region between 3.2 and 9.4 μm, while MIPS covers the region between 21.5 and 175 μm. The third instrument, the Infrared Spectrograph (IRS; Houck et al. 2004) provides

low and moderate-resolution spectroscopic capabilities (5 to 40 μm), although it has two small imaging peak-up apertures that can also be used for imaging.

The Infrared Array Camera (IRAC) is a simple four-channel camera that obtains simultaneous broad-band images at 3.6, 4.5, 5.8, and 8.0 μm. Two nearly adjacent 5.2×5.2 arcmin fields of view in the focal plane are viewed by the four channels in pairs (3.6 and 5.8 μm; 4.5 and 8 μm). All four detector arrays in the camera are 256×256 pixels in size (1.22 arcsec pixels), with the two shorter wavelength channels using InSb and the two longer wavelength channels using Si:As IBC detectors. IRAC is a general-purpose, wide-field camera that can be used for a large range of astronomical investigations. In-flight observations with IRAC have already demonstrated that IRAC's sensitivity, pixel size, field of view, and filter selection are excellent for studying numerous topics in galactic and extragalactic astronomy.

MIPS provides the long-wavelength coverage with imaging bands at 24, 70 and 160 μm at a spectral resolution of about 7% and very low resolution spectral energy distribution (SED) spectroscopy from 52 to 100 μm. MIPS uses true detector arrays of 128×128 pixels at 24 μm, 32×32 pixels at 70 μm, and 2×20 pixels at 160 μm, and achieves telescope limited resolution of 6, 18, and 40 arcsec at 24, 70 and 160 μm. For the first time, at these long infrared wavelengths, MIPS can achieve simultaneously high sensitivity, a large imaging field and the maximum possible angular resolution.

IRS consists of four separate spectrograph modules, known by their wavelength coverage and resolution as Short-Low (SL), Short-High (SH), Long-Low (LL) and Long-High (HL). Two Si:As array detectors (128×128 pixels) collect the light into the SL and SH modules., while two Si:Sb array detectors (128×128 pixels) are used in the LL and LH modules. IRS also contains tow peak-up imaging fields with bandpasses centered at 16 μm and 22 μm.

The *Spitzer Space Telescope* is managed by JPL for NASA. Science operations are conducted at the Spitzer Science Center at Caltech, Pasadena, CA.

Additional information on the *Spitzer Space Telescope* and its instruments can be found at the Spitzer Science Center (SSC) web site.[1]

3. A New View of Galaxy Morphology and Classification

The morphological classification scheme introduced by Hubble (1926, 1936), based on blue-light images, has been modified periodically over the years (e.g., Sandage 1961; de Vaucouleurs 1959; Kormendy 1979; Buta 1995) but remains a fundamental method by which astronomers continue to sort and compare galaxies. While the method has proven very successful over much of the last century, its dependence on fundamental, physical properties intrinsic to the galaxies is indirect due to the complicated emission processes sampled in the B-band.

Using recent observations from the IRAC instrument on the *Spitzer Space Telescope*, the morphological classification scheme using images with resolution and sensitivities similar to those used for traditional optical classifications, but at mid-infrared wavelengths, were achieved (Pahre et al. 2004b). While some nearby galaxies could be resolved by previous infrared space missions operating at these wavelengths, and equal or better spatial resolution can be obtained from the ground, the combined wide-field coverage and sensitive infrared imaging detectors of the IRAC instrument on the *Spitzer Space Telescope* permits us to explore an entirely new region of parameter space for imaging nearby galaxies. These images demonstrate a new approach to galaxy classification based on the properties of the galaxy *interstellar medium* relative to its starlight.

4. Observations

The galaxies presented here are a small but representative subset of a sample of about 100 scheduled to be observed with Spitzer. These galaxies were taken from a complete sample from Ho et al. (1997). The sample observed to date with *Spitzer* nearly fully spans the classical morphological sequence (only Sa is missing).

The data were taken with the Infrared Array Camera (IRAC; Fazio et al. 2004) on the *Spitzer Space Telescope* during the first five IRAC campaigns of normal operations (2003 December – 2004 April).

The general infrared SED properties of various galaxy components are shown in Figure 2, along with the IRAC filter bandpasses. Starlight is blue in the IRAC bandpasses, because the mid-infrared wavelengths are longer than the peak of the blackbody radiation even for cool M giant stars. (Note that M giants are *bluer* than Vega in the $[3.6] - [4.5]$ color due to CO absorption in the 4.5 μm bandpass.) Warm dust emission appears in lines of polycyclic aromatic hydrocarbon (PAH) molecules in the 5.8 and 8.0 μm bandpasses. Emission from an AGN is *redder* than starlight in the infrared bandpasses.

5. Infrared Morphologies of Galaxies

Images of the galaxies at 3.6 and 8.0 μm are shown in Figures 3 and 4, organized by optical morphological type. A color representation of the images at 3.6, 4.5, and 8.0 μm is shown at the end of this paper. The 3.6 μm flux samples the unreddened stellar light distribution, while the 8.0 μm flux samples that same starlight (dimmed by a factor of more than four since these wavelengths are on the Rayleigh-Jeans tail) plus emission lines of PAH tracing out warm dust.

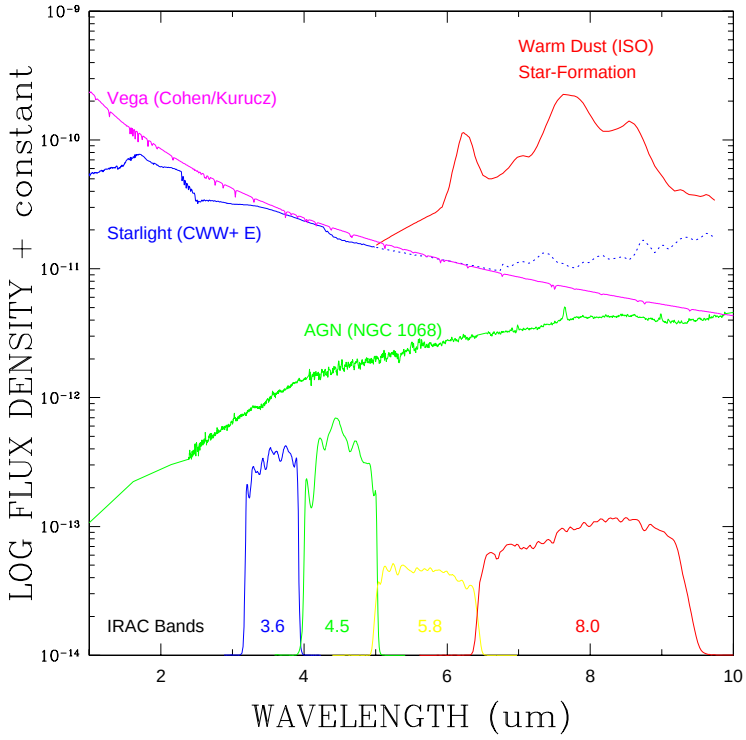

Figure 3. The spectral energy distributions of various galaxy components (starlight, warm dust, and active nuclei) at the IRAC wavelengths. The IRAC bandpasses are shown at the bottom of the figure. Warm dust emitting in the PAH lines, and active nuclei, both appear red in the IRAC bandpasses, while stellar light appears blue. The presence of CO absorption in the 4.5 μm bandpass also results in cool, late-type stars having a bluer color $[3.6]-[4.5]$ than earlier-type stars like Vega.

Comparing Figures 3 and 4, early-type galaxies and the bulges of spiral galaxies are dominated by starlight emission. The disks of late-type galaxies, on the other hand, are dominated by warm dust emission.

Galaxy morphology is more clearly delineated in the dust emission (Figure 4) than it is in the traditional, optical blue light images. The warm dust provides a clean tracer of the reddening-free interstellar medium, which has high contrast and can trace spiral arms all the way to the center of a galaxy. Furthermore, there is a changing ratio of starlight to warm dust emission along the galaxy sequence. This is the basis of a new method of classifying galaxies in the infrared at $3.2 < \lambda < 9.4$ μm using Spitzer images. This is shown graphically in the color fi gure appearing at the end of the volume (Figure 18), where the starlight is color-coded as blue and the warm dust as red.

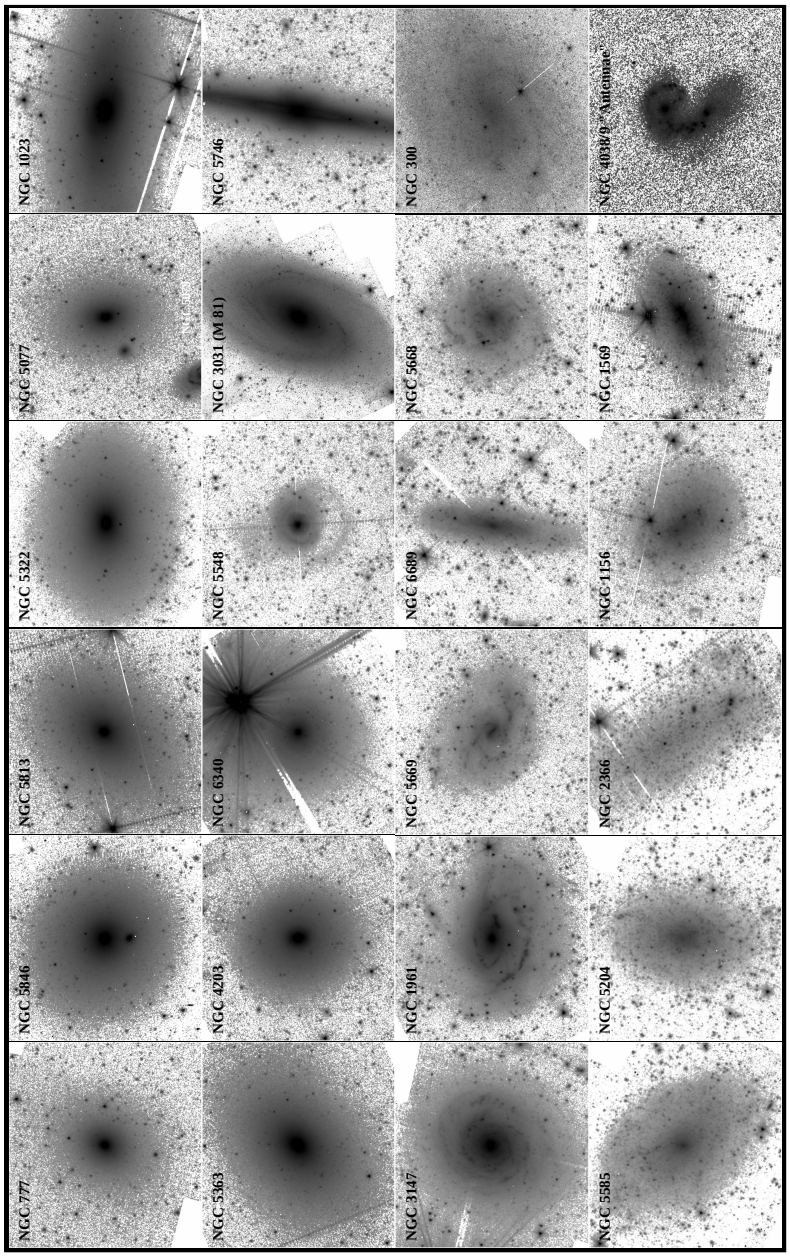

Figure 4. Images of the galaxies at $\lambda = 3.6$ μm. The mosaic is organized from early- to late-types from left to right.

Other IR quantities which correlate with optical morphological type are shown in Figure 5. Two colors correlate well: the stellar $[3.6] - [4.5]$ color

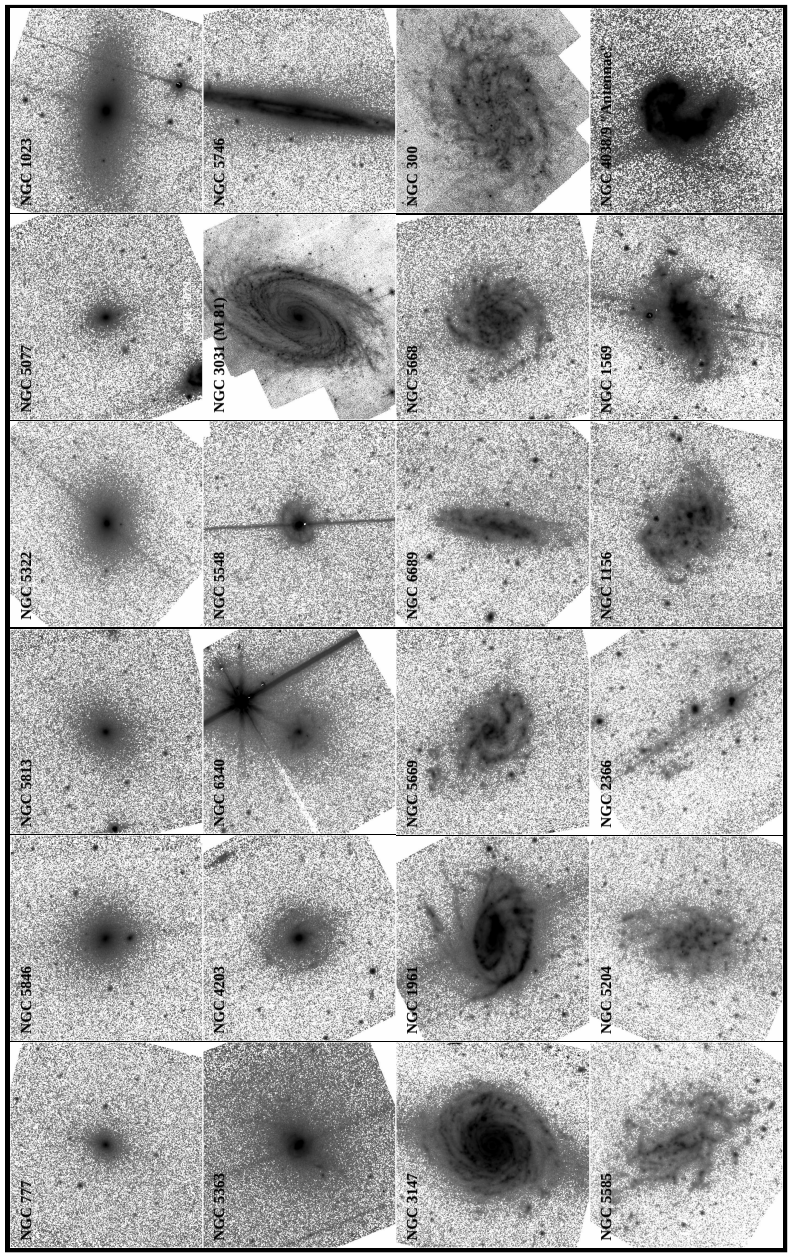

Figure 5. Images of the galaxies at $\lambda = 8.0\ \mu$m.

and the stellar vs. warm dust color $[3.6] - [8.0]$. The color $[3.6] - [4.5]$ is redder for late-type galaxies because they have a young stellar population that

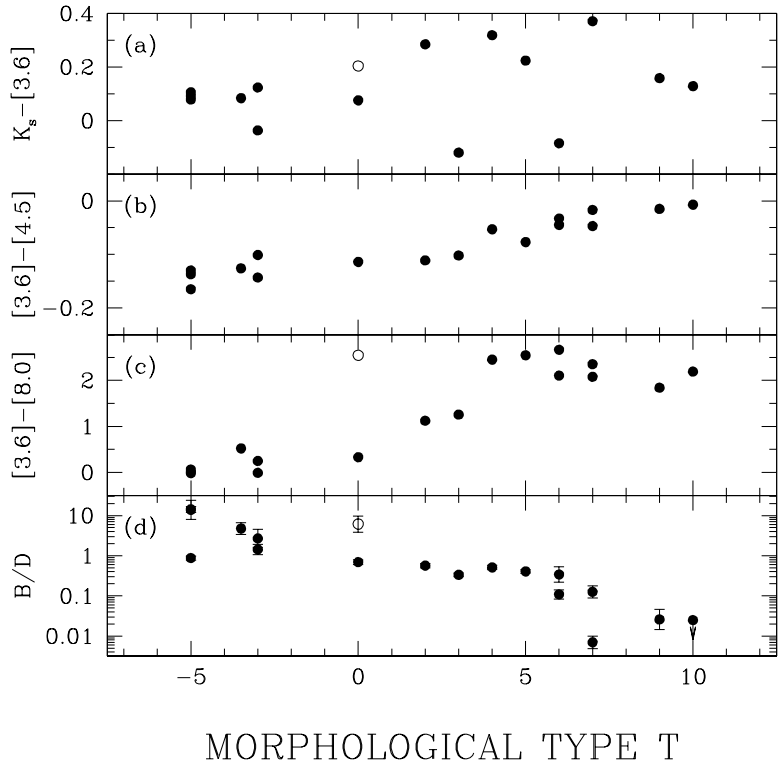

Figure 6. Correlation between various colors and the 3.6 μm bulge-to-disk-ratio with optical morphological type. The $[3.6]-[4.5]$ color shows that the starlight changes from blue for early-types to red for late-types. A similar trend is found for $[3.6]-[8.0]$, which samples the ratio of starlight to warm dust emitting at the longer wavelengths.

partially masks the the CO absorption, characteristic of late-type giant stars, in the 4.5 μm bandpass. (See Figure 2). The color $[3.6]-[8.0]$ is redder for late-type galaxies due to the warm dust emission in the PAH lines in the 8.0 μm bandpass. The IR bulge-to-disk ratio also shows a good correlation. Any of these quantities, or all of them together, are suitable stand-ins for galaxy morphological type.

Why do infrared morphological classifi cation and these other three quantities measured at infrared wavelengths work so well? The 3.6 and 4.5 μm light is a good tracer of stellar mass (for a wide range of metallicity and age) free of dust obscuration, hence B/D measured at these wavelengths samples a fundamental galaxy property. The dust emission is a high contrast tracer of the interstellar medium, thereby making the morphology easier to discern. In galaxies of various types, the 8.0 μm bandpass can exhibit anything from $\sim$ 100% starlight (elliptical galaxies) to $\sim$ 95% dust emission (NGC 1961,

3147, 4038/4039), and thus the $[3.6] - [8.0]$ color provides a direct measure of increasing ISM content along the galaxy sequence.

6. Spatial Distribution of Warm Dust in Lenticular Galaxies

The warm gas phase was detected in early-type galaxies via its dust emission at far-IR wavelengths with IRAS (Jura et al. 1987; Knapp et al. 1989) and at optical wavelengths from atomic gas emission (Caldwell 1984; Phillips et al. 1986). Later, ISO detected polycyclic aromatic hydrocarbon (PAH) lines in the mid-IR (Lu et al. 2003; Xilouris et al. 2004). Of order half or more early-type galaxies exhibit either far-IR dust or optical ionized gas emission, although the detection rate in the infrared could be lower if the effects of an AGN are removed (Bregman et al. 1998). Current knowledge of the distribution of warm dust emission within early-type galaxies indicates that it mostly follows the light distributions (e.g., Athey et al. 2002) and hence is thought to arise from processes other than star formation such as AGN mass loss. The exceptions to this statement are a few galaxies with somewhat extended structures in 15 μm ISO images that have been interpreted as dust lanes (Xilouris et al. 2004).

The mid-IR imaging capability of the Spitzer improves the spatial resolution over previous missions by a factor of a few and the sensitivity by more than an order of magnitude. These new images (Figure 7; Pahre et al. 2004a) show that several early-type galaxies have substantial structure in the distribution of their warm dust as traced by PAH emission bands at 6.2 – 8.6 μm. In particular, two lenticular galaxies show warm dust organized into spiral arms, and a third shows an extended, smooth distribution. For NGC 4203, this warm dust emission is not seen as obscuration at optical wavelengths with the Hubble Space Telescope (Erwin & Sparke 2003), further demonstrating the power of the infrared to highlight new galaxy morphological features that are invisible at optical wavelengths.

7. NGC 5746 at Infrared Wavelengths

A good example of the power of infrared galaxy classification is NGC 5746 (Figure 8), an edge-on spiral that cannot be reliably classified at optical wavelengths. Even the near-infrared emission from 2MASS shows a little bit of obscuration, but the near-IR light is otherwise mostly smooth. At mid-IR wavelengths, however, a bright ring appears along with several arms outside of it. The galaxy's suggested morphological type is Sab(r).

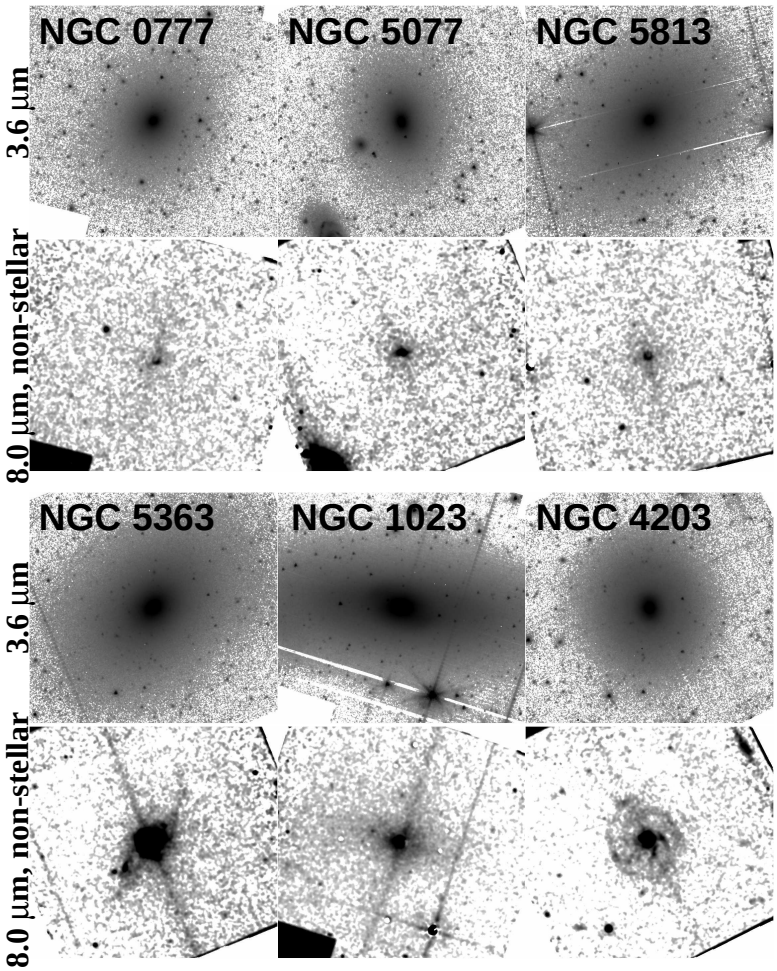

Figure 7. Warm dust emission in early-type galaxies. Six galaxies are shown, each with separate images in stellar emission (3.6 μm) and warm dust emission (8.0 μm "non-stellar"). The top three galaxies are classified as ellipticals and show no sign of warm dust emission at 8.0 μm. The bottom three galaxies are classified as lenticulars and show resolved warm dust. NGC 4203 appears face-on with several spiral arms emanating out from its nucleus, NGC 5363 appears somewhat inclined and shows two arms, and NGC 1023 shows a smooth distribution of dust.

8. Identifying the AGN in M 81

The presence of an AGN in M 81 can be inferred in two ways: (1) nuclear colors significantly redder than the bulge, and (2) point source residual after fitting and subtracting two-dimensional models of the bulge and disk light.

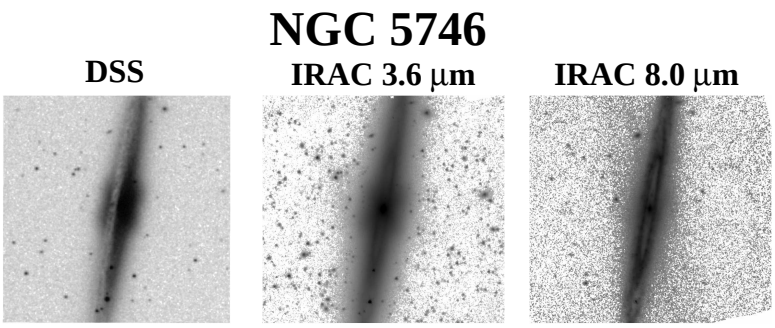

Figure 8. Edge-on spiral galaxy NGC 5746. At optical wavelengths (left), the galaxy shows a prominent dust lane. The IRAC image at 3.6 μm (middle) is free of dust obscuration and shows a hint of a spiral arm. The 8.0 μm image (right) shows the ring prominently as well as several arms outside of it, demonstrating that this is a Sab(r) galaxy. The ring and arms are prominent in the PAH emission lines in the 8.0 μm band.

The first one is shown in Figure 9, and both are described by Willner et al. (2004). The nucleus of M 81 is more than 0.4 mag redder than the inner bulge, which cannot be explained by any reasonable stellar photosphere model.

9. Summary of Spitzer Results on Galaxy Morphology and Classification

Images of two dozen galaxies taken at $3.2 < \lambda < 9.4$ μm with the IRAC instrument on the *Spitzer Space Telescope* show that:

1 The mid-IR clearly separates emission from interstellar matter and starlight without the effects of extinction.

2 The mid-IR dust emission, particularly the PAH feature at $\lambda = 7.7$ μm, is a clear tracer of the presence of interstellar matter. The emission shows high contrast against stellar emission at the same wavelength.

3 The mid-IR light provides an entirely new scheme by which to classify galaxies–primarily based on the ratio of their ISM to starlight emission.

4 The colors of stellar photospheres in the mid-IR vary only a small amount with population age or mass function, and hence the stellar emission is a direct tracer of stellar mass. The bulge-to-disk-ratios measured at 3.6 and 4.5 μm therefore sample the mass ratio of the stellar content, not a mixture of stellar content and recent massive star formation activity.

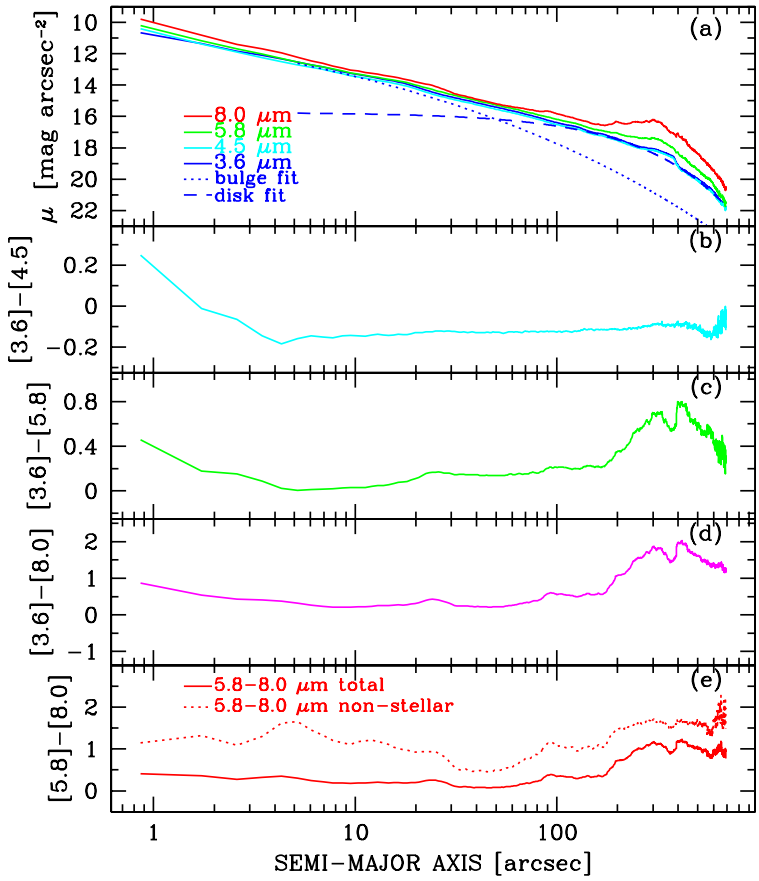

Figure 9. Surface photometry and color profiles for M 81. (a) Surface photometry in the IRAC bands along with bulge plus disk model fit to the 3.6 μm data. (b) Color profile in $[3.6]-[4.5]$ which shows $+0.4$ mag redder colors in the nucleus, indicative of an AGN. (c) and (d) Color profile in $[3.6]-[5.8]$ and $[3.6]-[8.0]$, which are both redder than starlight alone due to PAH emission at the long wavelengths. (e) Color profiles in $[5.8]-[8.0]$ for both the combined starlight and warm dust and the warm dust alone. The color of the warm dust is roughly consistent with PAH color $[5.8]-[8.0]=2.06$ mag predicted by Li & Draine (2001).

5 Two colors ($[3.6]-[4.5]$ and $[3.6]-[8.0]$), as well as the 3.6 μm bulge-to-disk-ratio, correlate well with traditional morphological type and hence can be regarded as a means of galaxy classifi cation.

6 Three of six early-type galaxies observed exhibit dust emission that is organized into spiral arm or inner disk-like structures,

7 The $[5.8] - [8.0]$ color of the dust emission matches that for dust in actively star-forming galaxies and theoretical models of PAH emission, and

8 Active galactic nuclei can be readily identified both via their mid-infrared colors and as point source residuals in two-dimensional modelling.

10. Star Formation in Colliding Galaxies: The Antennae

Imaging of the Antennae galaxies (NGC 4038/4039) with IRAC has revealed large concentrations of star-forming activity away from both nuclei of the two merging galaxies (Wang et al. 2004) and confirm earlier ISO observations with lower resolution (Viguroux et al. 1996; Mirabel et al. 1998). IRAC images (Figure 10) have provided a new view of the total underlying star-forming activities unaffected by dust obscuration. The local star formation rate in the Antennae, using the flux ratio of non-stellar to stellar emission as measured by IRAC, can be mapped and compared to the measurements in starburst and ultraluminous galaxies. The rate in the active regions of the Antennae is found to be as high as those observed in starburst and ultraluminous galaxies on a "per unit mass" basis. This more complete picture of star formation in the Antennae will help us better understand the evolution of colliding galaxies, and the eventual fate of our own galaxy.

11. Spitzer Observations of Young Stellar Clusters

The *Spitzer Space Telescope* promises to further revolutionize the study of star formation by providing the capability to image young stellar groups and clusters at mid-infrared wavelengths with the sensitivity to detect young stars down to the hydrogen burning limit and below. With this new capability, the legacies of IRAS, ISO and numerous ground-based near-infrared observations can be expanded by probing the spectral energy distributions of stars, brown dwarfs and protostars in young stellar clusters out to distances of 1 kpc or greater.

The IRAC team has imaged 31 young stellar groups and clusters with the MIPS and IRAC instruments. These have been selected from a catalog of 63 star forming regions within 1 kpc of the Sun containing 10 or more members (Porras et al. 2003). In parallel, 7 square degrees in the Orion molecular clouds are also being mapped. These surveys will sample the full continuum of multiple star forming regions in the nearest kiloparsec, from small groups of stars in Taurus to the rich Orion Nebula and Mon R2 clusters.

Initial results for four young stellar clusters in our sample with properties between those of Taurus and Orion: S140, S171, Cepheus C, and NGC 7129 have been reported by Megeath et al. (2004). These regions are at similar

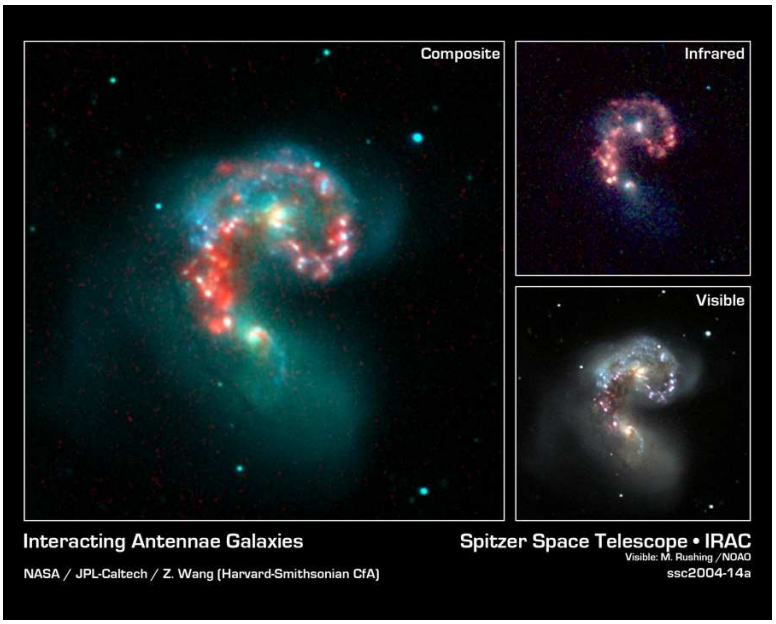

Figure 10. Interacting Antennae Galaxies (NGC 4038/4039). The left image is a false-color composite of IRAC data and visible-light data from Kitt Peak National Observatory (M. Rushing). Visible light from stars in the galaxies (blue and green) is shown together with infrared light from warm dust clouds heated by newborn stars (red). The two nuclei of the merging system show up as yellow-white areas, one above the other. The upper right image shows the IRAC image by itself, with 3.6 μm wavelength in blue, 4.5 μm in green, 5.8 μm in orange and 8.0 μm in red. The lower right image shows the true-color, visible-light image by itself. Note in this image that the bright star-forming regions seen in the infrared image are blocked by dust clouds in the optical image.

distances, but span a range of FIR luminosities, molecular gas masses, and cluster membership. In each cluster, color-color diagrams, based on IRAC photometry, were used to identify young stars with disks and protostars (Figure 11). Classifi cation was based on the results of a paper by Allen et al. (2004) in which the IRAC colors of the observed young stars are compared to colors derived from models of stars with disks or infalling envelopes. In each of the four clusters, there are between 39 and 85 objects with colors inconsistent with reddened stellar photospheres.

12. The Distribution of Young Stars

We show IRAC mosaics of all four clusters in Figures 12 and Figure 13. In preparation for the *Spitzer* young stellar cluster survey, Ridge et al. (2003) mapped each of these regions in the ^{13}CO and C^{18}O ($J = 1 \rightarrow 0$) transition. overlay contours of the the C^{18}O emission, which is an excellent tracer of the

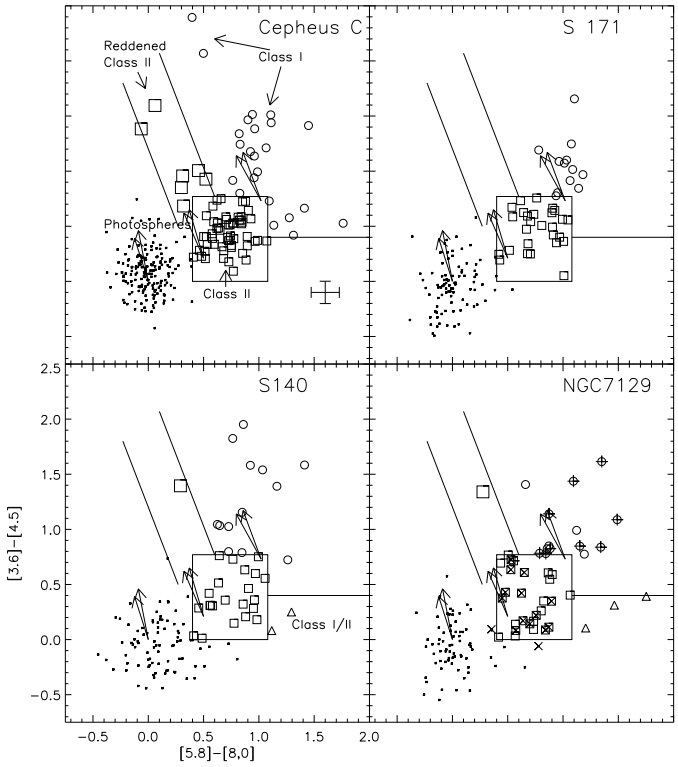

Figure 11. The IRAC color-color diagram is displayed for all four clusters. Using a selection criteria outlined in the text and in Allen et al. 2004, the squares are identified as class II sources, the large square are reddened class I sources, and the circles are class I sources. The two parallel lines border the positions of sources we identify as reddened class II objects. In two of the regions, S140 and NGC 7129, we mark the class I/II sources (which share the characteristics of both class I and class II sources) with triangles; the horizontal line above the triangles shows the adopted division between class and class I/II sources. We show reddening vectors for $A_V = 30$ derived from the Draine & Lee (1984) and Mathis (1990) extinction laws, in each case the Draine & Lee vector points to the left of the Mathis vector. The vectors were calculated for Vega (at position 0,0), a young star with disks taken from the models of D'Allessio et al. (2004) (0.2,0.5), and a flat spectrum source (0.73,1). Twenty-four sources in NGC 7129 were classified using IRAC photometry combined with MIPS 24 μm photometry by Muzerrole et al. (2004); to display these classifications we overplot a plus sign for class I objects and an X for class II objects. The error bars in the Cepheus C plot show the median uncertainty in the colors for all the sources in all four clusters. A conservative 0.1 mag calibration uncertainty was added in quadrature to the median photometric uncertainty.

structure of the molecular gas in star forming regions (Goldsmith, Bergin & Lis 1997). We find 72% of the class I and 56% of the class II sources fall within the detected $C^{18}O$ emission, and 93% of the class I and 86% of the class II sources fall within the detected ^{13}CO emission. These percentages are

qualitatively consistent with the class I sources being younger than the class II sources.

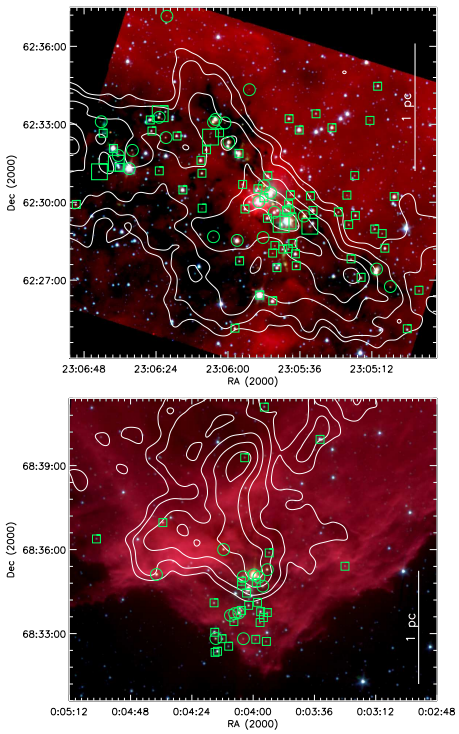

Figure 12. Images of Cepheus C (top) and S171 (bottom) constructed from the IRAC 3.6 μm (blue), 4.5 μm (green) and 8.0 μm (red) images. The contours are the maps of $C^{18}O$ ($1 \rightarrow 0$) emission from Ridge et al. (2003). The $C^{18}O$ observations have an angular resolution of $50''$. We show the position of each young star identified in the IRAC color-color diagram. We mark class II sources with squares, reddened class II objects with large squares, and class I objects with circles. The class I/II sources are marked by triangles.

13. Summary of Spitzer Observations of Young Stellar Clusters

In all four clusters, the very young stars and protostars were identified by their excess emission in the mid-infrared and their distribution over multi-parsec distances was determined. In contrast, the diameters of the clusters identified by near-IR star counts are typically 1 pc or less (Lada et al. 2003). This suggests that a significant fraction of stars in each star forming region form outside the dense clustered regions identified in star counts analyses. Gutermuth et al. (2004) find that half of the stars in NGC 7129 are located

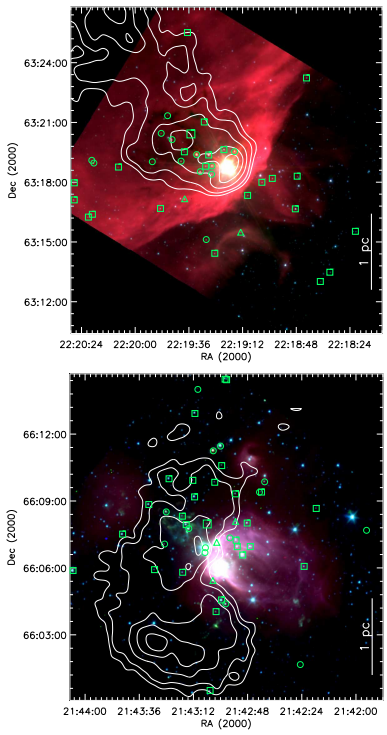

Figure 13. Images of S140 (top) and NGC 7129 (bottom) using the the same scheme described in Figure 12.

in a halo outside the cluster core. Furthermore, star formation in NGC 7129 is continuing in the halo, while the molecular gas has been dispersed toward the cluster core.

The distribution of sources in each region is strikingly different. In Cepheus C, the structure of the molecular cloud breaks up into distinct mid-IR dark cores, and several distinct concentrations of stars are also apparent to the eye. The observed distribution of gas and stars in this region is similar to the hierarchical morphologies generated in numerical models of star formation in turbulent clouds (Bonnell, Bate & Vine 2003). IRAC images of NGC 7129 show a dense cluster of primarily class II sources surrounded by a more extended halo of class I and II objects. Both S171 and S140 contain compact clusters at the edges of bright-rimmed clouds. These varied morphologies hint that environmental factors, such as the presence of external OB stars, may play a signifi cant role in the formation of clusters.

14. Spitzer Reveals a Molecular Outflow from a Low Mass Protostar

Jets and outflows arising from low mass protostars can produce some of the most spectacular images of the star formation process. The HH 46/47 system is a striking example of a low mass protostar, surrounded by a circumstellar disk, ejecting a jet and creating a bipolar outflow perpendicular to the disk (Figure 14). The central protostar lies inside a dark cloud (known as a Bok globule) which is illuminated by the nearby Gum Nebula. At a distance of 450 pc in the constellation Vela, the protostar is hidden from view in the visible–light image (inset, Figure 14). When observed with IRAC the star and its dazzling jets of molecular gas appear with clarity (Noriega-Crespo et al. 2004). The clear definition of the counterlobe, similar to a large loop, which joins the bow shock with the source, is the most remarkable feature of the picture. For the first time the complete picture of the outflow at mid-infrared wavelengths is revealed. The jets arising from such protostars can reach sizes of trillions of kilometers and velocities of hundred of thousands of kilometers per hour.

A spectrum of HH 46/47, taken with the IRS's Short-Low and Long-Low Infrared Spectrometers over the wavelength range from 5.5 to 20 μm, is shown in Figure 15. Detected in the spectrum are water and carbon dioxide ices, silicates, and organic molecules, such as methyl alcohol and methane gas, which are thought to exist in the circumstellar disk surrounding the protostar. Observations of ices around low-mass protostars have been limited because of the unavailability of much of the 5-20 μm spectral region, where many of the molecular bending-mode transitions occur. For the first time, using *Spitzer*, high quality spectra can now be obtained in low-mass protostellar systems.

15. Ring of Stellar Death

Shown in Figure 16 (Hora et al. 2004) is a false color image from *Spitzer* of the planetary nebula NGC 246, a dying star (center) surrounded by a cloud of glowing gas and dust which has been ejected from the star. Because of *Spitzer's* ability to penetrate the dust, this image highlights a never-before-seen feature: a giant ring of material slightly offset from the cloud's core. It is believed the ring consists of molecular hydrogen molecules that were ejected from the star in the form of atoms, then cooled to make hydrogen molecules. This new data will help explain how planetary nebulae take shape and eject matter into the interstellar medium.

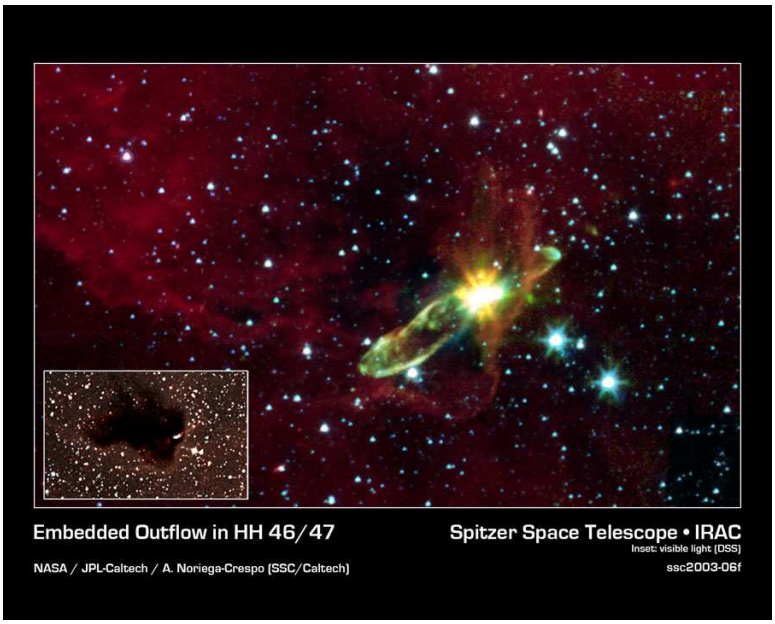

Figure 14. Image of the HH 46/47 system arising from the Bok globule (ESO 210-6A) obtained with IRAC. The image covers a region of approximately 6.5×10.6 arcmin. Emission at 3.6, 4.5 and 5.8, and 8.0 μm is shown as blue, green, and red, respectively. The inset is a visible light comparison image.

16. A Portrait of Life and Death in the Universe: Henize 206

A wonderful example of the cycle of life and death that gives rise to stars throughout the universe is demonstrated in the *Spitzer* image of the nebula Henize 206 (He 206), which is located in the Large Magellanic Cloud (Figure 17). It is similar in size the the belt and sword of Orion, but is about 10 times as luminous in the infrared. Henize 206 was created when a supernova exploded, sending shock waves which impacted a molecular cloud of gas and dust, causing stars to be formed. The supernova remnant is seen as a ring of shocked gas, which is green in the figure. By mapping in the infrared, *Spitzer* was able to see through blankets of dust in the molecular cloud that block visible light and view the embedded young stars (bright white spots) that were formed as a result of the impact (V. Gorjian et al. 2004). Before the *Spitzer* observations there were only hints that newborn stars may be present.

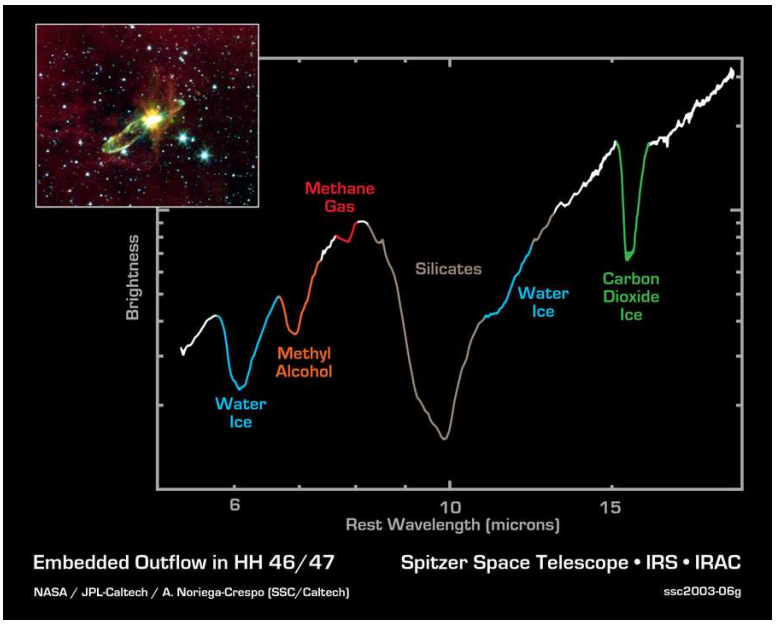

Figure 15. A spectrum of HH 46/47 obtained with IRS from 5.5 to 20 μm.

17. Summary

The *Spitzer Space Telescope* has been operating very successfully since it started routine observations in December, 2003. The sample of new scientific results presented in this paper are indicative of its future potential for discovery over the next five years. The *Spitzer Space Telescope* is designed for the entire scientific community and all are urged to use it to expand our knowledge of the universe.

Acknowledgments

This work is based on observations made with the *Spitzer Space Telescope*, which is operated by the Jet Propulsion Laboratory, California Institute of Technology under NASA contract 1407. Support for the IRAC instrument was provided by NASA through Contract Number 960541 issued by JPL. The IRAC GTO program is supported by JPL Contract # 1256790. IRAF is distributed by the National Optical Astronomy Observatories, which are operated by the Association of Universities for Research in Astronomy, Inc., under cooperative agreement with the National Science Foundation. This publication makes use of data products from the Two Micron All Sky Survey, which is a joint project of the University of Massachusetts and the Infrared Processing and Analysis Center/California Institute of Technology, funded by the Na-

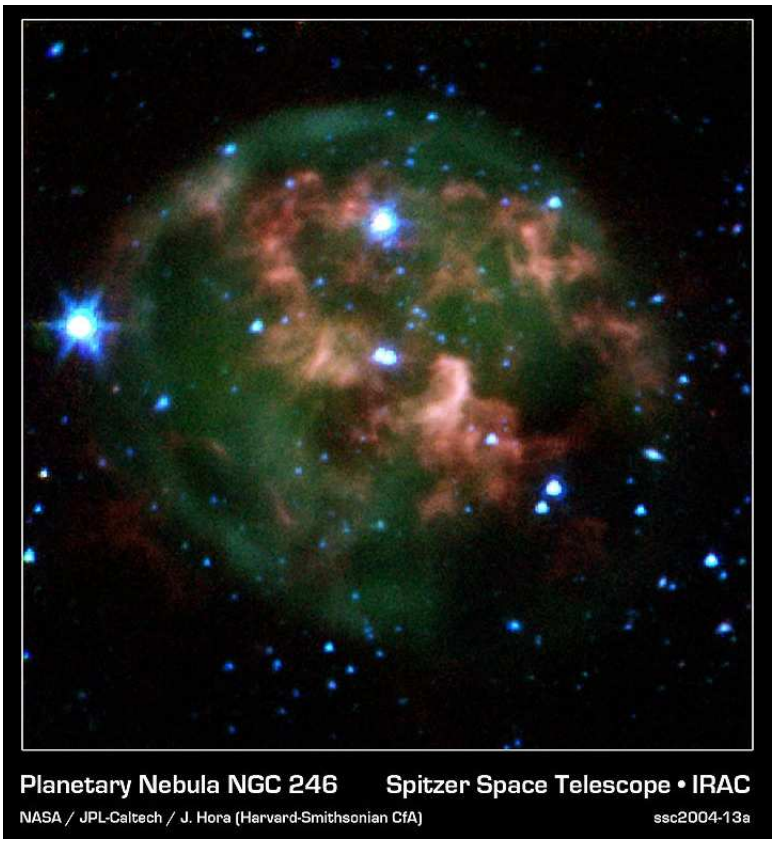

Figure 16. The planetary nebula NGC 246.

tional Aeronautics and Space Administration and the National Science Foundation. This research has made use of the NASA/IPAC Extragalactic Database (NED) which is operated by the Jet Propulsion Laboratory, California Institute of Technology, under contract with the National Aeronautics and Space Administration. The Digitized Sky Surveys were produced at the Space Telescope Science Institute under U.S. Government grant NAG W-2166.

Notes

1. http://www.spitzer.caltech.edu

References

Allen, L. E., Calvet, N., D'Alessio, P., Merin, B., Megeath, S. T., Gutermuth, R. A., Pipher, J. L., Hartmann, L., Myers, P. C., & Fazio, G. G. 2004, ApJS, 154, 363.

Athey, A., Bregman, J., Temi, P., & Sauvage, M. 2002, ApJ, 571, 272.

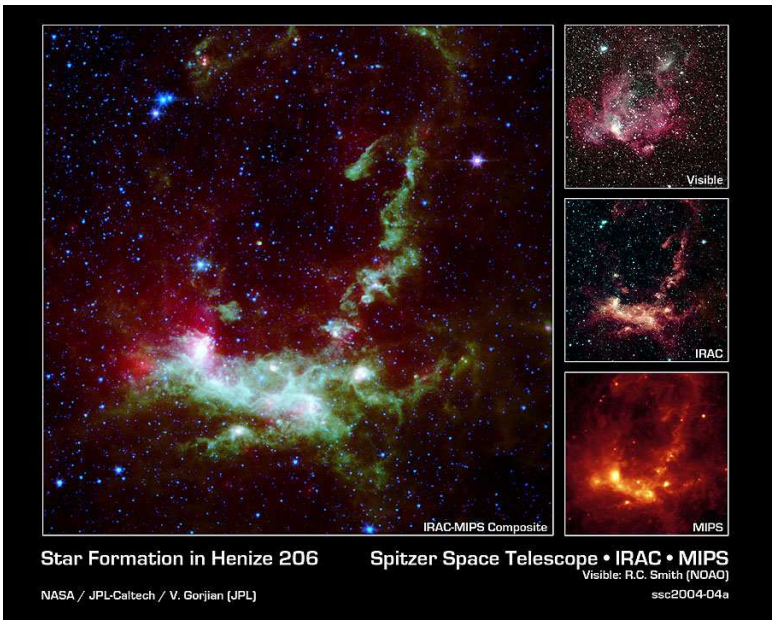

Figure 17. Henize 206 in the Large Magellenic Cloud.

Bonnell, I. A., Bate, M. R., & Vine, S. G. 2003, MNRAS 343, 413.
Bregman, J. N., Snider, B. A., Grego, L., & Cox, C. V. 1998, ApJ, 499, 670.
Buta, R. 1995, ApJS, 96, 39.
Caldwell, N. 1984, PASP, 96, 287.
D'Alessio, P., Merin, B., Calvet, N. & Hartmann, L. 2004, in preparation.
de Vaucouleurs, G. 1959, Handbuch der Physik, 53, 275.
Draine, B. T. & Lee, H. M. 1985, ApJ, 290, 211.
Erwin, P. & Sparke, L. S. 2003, ApJS, 146, 299.
Fazio, G. G., et al. 2004, ApJS, 154, 10.
Goldsmith, P. F., Bergin, E. A. & Lis, D. C. 1997, ApJ, 491, 615.
Gorjian, V., et al. 2004, ApJS, 154, 275.
Gutermuth, R. A., Megeath, S. T., Allen, L. E., Muzerolle, J., Pipher, J. L., Myers, P. C., & Fazio, G. G. 2004, ApJS, 154, 374.
Ho, L. C., Filippenko, A. V., & Sargent, W. L. W. 1997, ApJS, 112, 315.
Hora, J. L., Latter, W. B., Allen, L. E., Marengo, M., Deutsch, L. K., & Pipher, J. L. 2004, ApJS, 154, 296.
Houck, J. R., et al. 2004, ApJS, 154, 18.
Hubble, E. P. 1926, ApJ, 64, 321.
Hubble, E. P. 1936, Realm of the Nebulae (New Haven: Yale University Press).
Jura, M., Kim, D. W., Knapp, G. R., & Guhathakurta, P. 1987, ApJ, 312, L11.
Knapp, G. R., Guhathakurta, P., Kim, D., & Jura, M. A. 1989, ApJS, 70, 329.
Kormendy, J. 1979, ApJ, 227, 714.
Lada, C. J. & Lada. E. A. 2003, ARAA, 41, 57.

Li, A. & Draine, B. T. 2001, ApJ, 554, 778.

Lu, N., et al. 2003, ApJ, 588, 199.

Megeath, S. T., Allen, L. E., Gutermuth, R. A., Pipher, J. L., Myers, P. C., Calvet, N., Hartmann, L., Muzerolle, J. & Fazio, G. G. 2004, ApJS, 154, 367.

Mathis, J. S. 1990, ApJ, 28, 37.

Mirabel, I. F. et al. 1998, A&A, 333, L1.

Muzerolle, J., Megeath, S. T., Gutermuth, R. A., Allen, L. E., Pipher, J. L., Gordon, K. D., Morrison, J. E., Rieke, G. H., Myers, P. C., & Fazio, G. G. 2004, ApJs, 154, 379.

Noriega-Crespa, A. et al. 2004, ApJS, 154, 352.

Pahre, M. A., Ashby, M. L. N., Fazio, G. G., & Willner, S. P. 2004a, ApJS, 154, 229.

Pahre, M. A., Ashby, M. L. N., Fazio, G. G., & Willner, S. P. 2004b, ApJS, 154, 235.

Phillips, M. M., Jenkins, C. R., Dopita, M. A., Sadler, E. M., & Binette, L. 1986, AJ, 91, 1062.

Porras, A., Christopher, M., Allen, L., Di Francesco, J., Megeath, S. T., Myers, P. C., 2003, AJ, 126, 1916.

Ridge, N. A.. Wilson, T. L., Megeath, S. T., Allen, L. E., Myers, P. C. 2003, AJ, 126, 286.

Rieke, G. H., et al. 2004, ApJS, 154, 25.

Sandage, A. 1961, The Hubble Atlas of Galaxies (Washington: Carnegie Institution).

Viguroux, L. et al. 1996, A&A, 315, L93.

Wang, Z., et al. 2004, ApJS, 154, 193.

Werner, M. W., et al. 2004, ApJS, 154, 1.

Willner, S. P., et al. 2004, ApJS, 154, 222.

Xilouris, E. M., Madden, S. C., Galliano, F., Vigroux, L., & Sauvage, M. 2004, A&A, 416, 41.

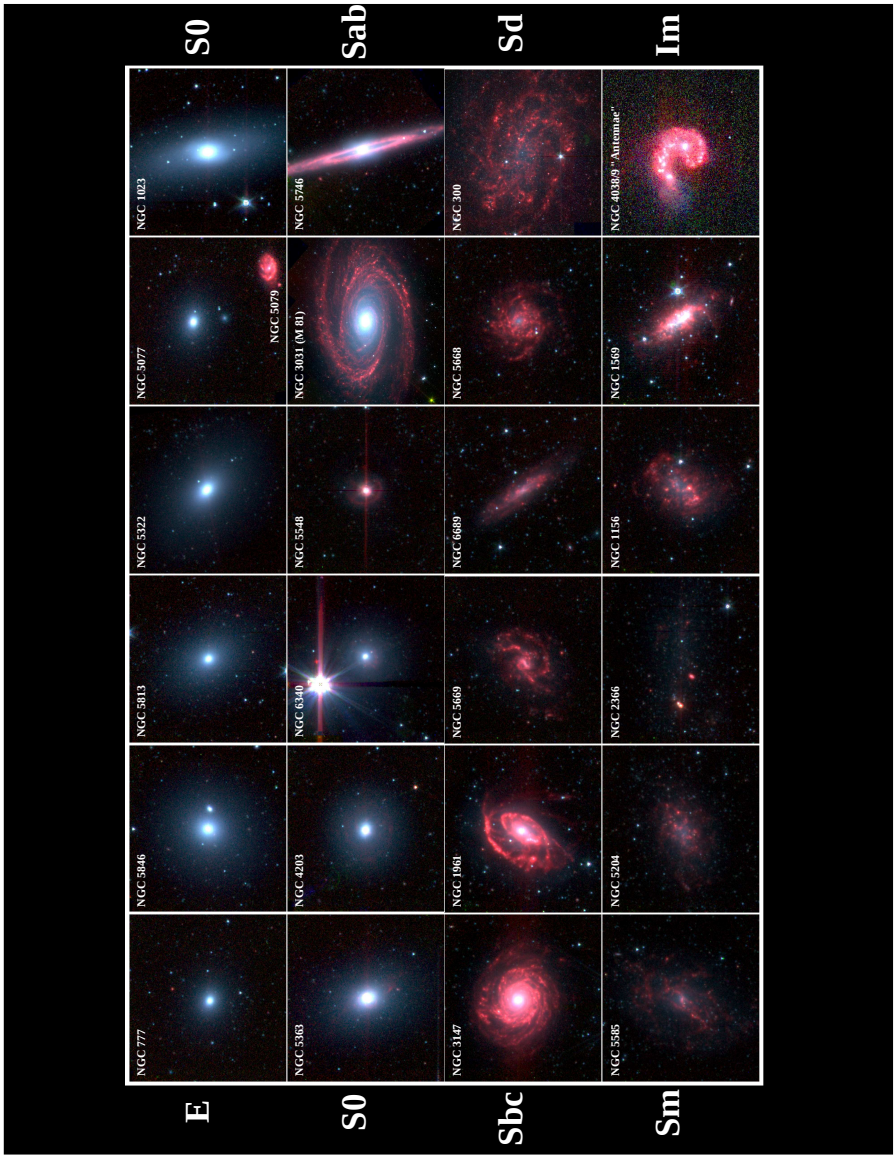

Figure 18. Mosaic of galaxies at infrared wavelengths taken with the IRAC instrument on the Spitzer Space Telescope. Colors are coded as 3.6 (blue), 4.5 (green), and 8.0 μm (red). The galaxies are arranged according to traditional, optical morphological classifications. Starlight appears blue at these mid-infrared wavelengths, while warm dust (emitting in PAH emission lines) appears red. AGN emission is also red and point-like (e.g., NGC 5548). There is a clear transition from blue, stellar-dominated emission for the early-type galaxies to red, ISM-dominated emission for the late-type galaxies.